AN INVESTIGATION ON DISSIMILAR THICKNESS AUSTENITIC STAINLESS STEEL PLASMA ARC WELDS USING FINITE ELEMENT METHOD

B. Chinna Ankanna [1, a)], K. Govindarajulu [2]

[1]Research Scholar, Department of Mechanical Engineering, Jawaharlal Nehru Technological University Ananthapuramu, Ananthapuramu-515002, Andhra Pradesh, India; Working at Rajeev Gandhi Memorial College of Engineering and Technology, Nandyal, Andhra Pradesh 518501, India.

[2]Professor, Department of Mechanical Engineering, Jawaharlal Nehru Technological University College of Engineering Ananthapuramu, Ananthapuramu-515002, Andhra Pradesh, India.

Abstract: A biomaterial is a matter that has been bring about to interact with biological systems for a medical purpose, either a therapeutic such as treatment, enhance, repair, or replace a tissue function of the body or a diagnostic one. Several metals, ceramics and polymers used as biomaterials. Metals are nominated for biomedical applications due to its properties such as biomechanical characteristics, surface finishing characteristics. Moreover, finite element models provide a detailed insight of several issues where experimental investigations not enough to understand. In the present work, a three-dimensional thermal model based on conduction heat transfer is developed to predict the thermal behavior during arc welding of austenitic stainless-steel plates of different thickness. The novelty of the present work is modeling of dissimilar plate thickness joining using finite element method. Moreover, double ellipsoidal power density model of Gaussian distribution is selected along with appropriate incorporation of material responses as a function of temperature for carrying out thermal analysis. Based on numerical results, it is determined that the developed process model is highly efficient in estimating thermal responses such as temperature history, weld profile and weld dimensions for dissimilar thickness plates joining.

Key words: Arc Welding, Dissimilar Plate Thickness, Austenitic Stainless Steel and Volumetric Heat Source.

1. INTRODUCTION

Though, austenitic stainless-steel material used as biomaterial, it is furthermore utilized in the manufacture of medical devices. Austenitic stainless steel is observed the world over as one of the most appropriate material for the manufacture of medical devices for all sorts of applications due to its unique material characteristics such as rust proof, high corrosion resistance, recyclable, antibacterial properties, high heat resistance etc. at an economical price point. Thus, making with stainless steel is the logical choice for medical device specification. Arc welding process is a reliable fusion welding method of coalescence between similar or dissimilar metallic structures for permanent and instant joints. Typical chemical composition and mechanical properties of austenitic stainless steel stainless steel for medical applications are given in table 1 and 2. Plasma Arc Welding process is one of the most emerging arc welding technique for joining aluminium and several other non-ferrous materials. Metallic materials have high module of physical property that limits stress distribution from implant to bone. Hence, “new aluminiferous parts are

developed with lower modulus and better corrosion and wear resistance. There's continuous analysis for brand new aluminiferous alloys for application in hip prostheses to get a higher biocompatibility at the side of superior mechanical properties. Still, it's obligatory to seek out a compromise between the various optimum characteristics desired for associate degree implant material" [1]. In figure 1, it's potential to envision the look of metal implants with completely various material adaptations [1].

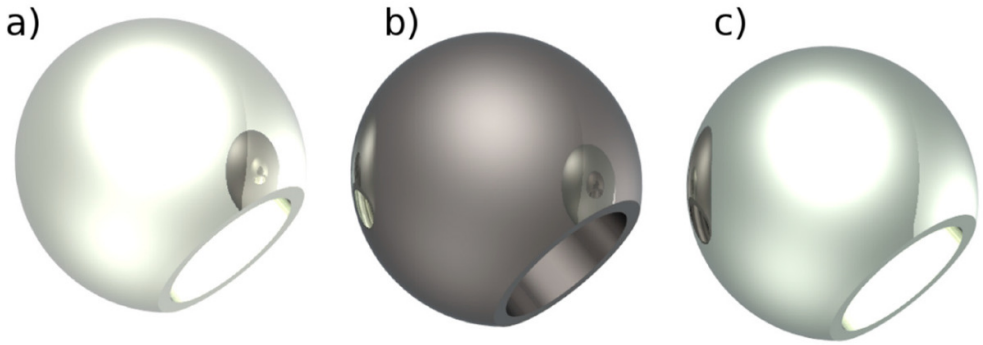

Figure 1: Femoral heads with different metals: (a) SS, (b) Oxinium and (c) CoCrMo [1].

Other foremost helpful biomaterials include Co alloys, stainless-steel, polymers, ceramics, etc. "With the aim of replace, support, stimulate and fix biological systems of humans, biomaterials are built for medical science implants, joints replacement, intraocular lenses, ligaments, heart valves, dental fixtures and implants, surgical mesh, pins and screws for fracture stabilization and stents across the body" [2]. The location of HIP replacement with metals is presented schematically in figure 2 [2].

Table 1: Chemical composition of austenitic stainless steel for medical applications

Element	Carbon (C)	Manganese (Mg)	Phosphorus (P)	Sulphur (S)	Silicon (Si)	Chromium (Cr)	Nickel (Ni)	Nitrogen (N)	Iron (Fe)
Wt.%	0.07 max.	2.00 max.	0.045 max	0.015 max.	0.75 max.	18 to 19.5	8 to 10.5	0.10 max.	Balance

Table 2: Typical mechanical properties of austenitic stainless steel for medical applications.

Property	Tensile strength (MPa)	Yield Strength 0.2% proof (MPa)	Elongation (% in 50 mm)	Hardness	
				Rockwell B (HR B)	Brinell (HB)
Value	540 min.	250 Min.	45 min.	92 max.	201 max.

Several noticeable applications of biomedical devices and applications of metals that are associated with welding processes are presented in the literature [3-10]. Figure3 describes the application of different welding processes in biomedical applications [3 and 6] such as manufacturing of biomedical devices, orthopedic and prosthetic implants etc. Figures 3 (a) to (e) refers to framework before sectioning, I-section design, frame work after laser welding, framework after TIG welding and terminology of prosthetic components. Figure 3 (f) depicts the repaired clasp with

hook to connect to existing clasps. Repaired clasp connected using laser welding and repaired prosthesis are shown in figure 3 (g) and 3 (h).

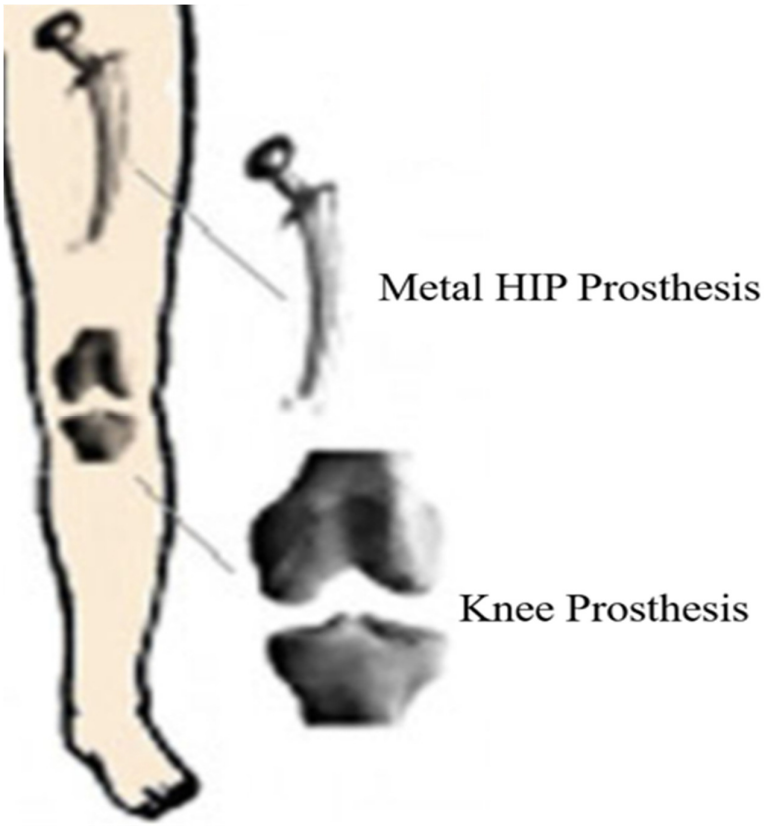

Figure 2: Applications of metals for human HIP prosthesis [2]

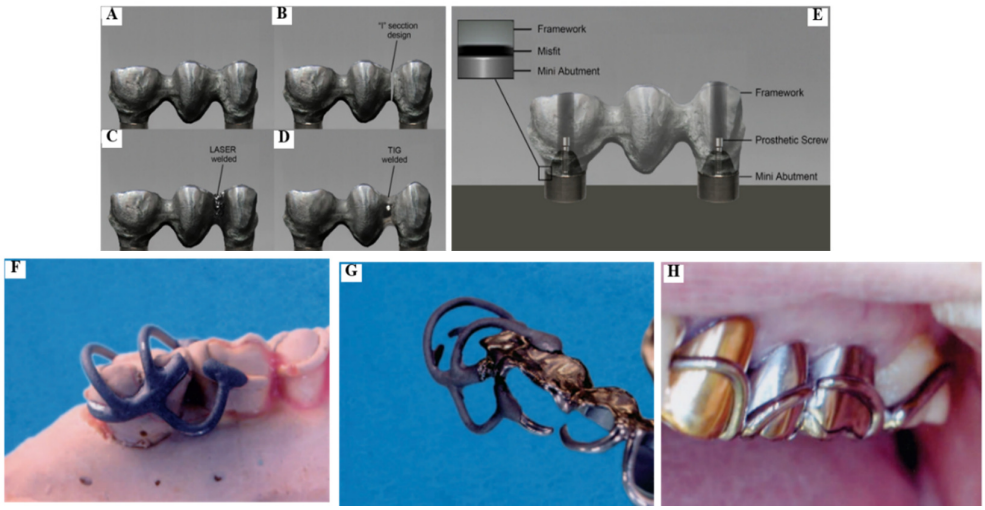

Figure 3: Applications of welding in biomedical applications: (a) framework before sectioning, (b) I-section design, (c) frame work after laser welding, (d) framework after TIG welding, (e) terminology of prosthetic components, (f) repaired clasp with hook to connect to existing clasps, (g) repaired clasp connected using laser welding and (h) repaired prosthesis [3 and 6].

Stainless steel was the first class of alloy introduced for orthopaedic implants. Though, some corrosion was inevitable, it has been suggested that stainless steel only be used for short duration purposes. Plasma arc welding (PAW) is a high energy density joining process which generates higher arc temperature and it can be performed at higher arc velocity when compared with conventional joining methods such as gas tungsten arc and gas metal arc welding processes. With an aim to reduce the experimental trials of optimizing of weld variables and to determine weldments having higher joint integrity, a mathematical numerical model will serve the purpose significantly. In PAW process, joining of metals is achieved from the heat of an arc which is produced between a continuously feed filler metal electrode and the work material. The intense heat is generated due to arc carrying electric current. The shielding gas which comprises of active or inert gas or a gas mixture is ionized in its plasma phase, The periodically generated droplets due to the effect of high temperature plasma will melt the filler-metal electrode. Due to the combined influence of plasma flow and impingement of droplet, weld pool formation on the work-piece will initiate [11-12]. Moreover, in order to make implants for short duration, the plasma arc welding process can be explored due its advantages.

The weld parameters plays a key factor in deciding the quality of weldment. Therefore, in order to get the most appropriate and optimised process parameters, it is crucial to comprehend the thermal process involved during arc welding procedure. Temperature distribution analysis usually involve Finite Element Method (FEM). The first step involved towards predicting temperature distribution using FEM technique is to select the most appropriate heat source model for the arc joining procedure. In this aspect, Ibrahim et al. [11] examined the influence of arc welding variables such as welding current, arc voltage and welding speed on overall weld quality. The authors determined that with increase in welding current, the weld penetration is increased. In fact, the weld penetration is subjective to welding speed and arc voltage. Guo et al. [12] has examined the carter formation in 6005-T4 aluminium alloy using mathematical modelling. The authors determined that the crater formation in weldment is because of droplet impingement effect and arc pressure. An integrated 3D comprehensive model is developed by Xu et al. [13] to examine the transport phenomena during GMA joining process. The developed model is capable of efficiently computing magnetic and electric field for the entire solution domain.

Francis et al. [14] performed welding simulation using FEM method for a butt section welded joint and a tee section welded joint of aluminium alloys. The butt-welding simulation were performed for a single weld pass while tee section welding simulation were carried out for two weld passes. From the computational results, it was determined that for a tee section weld joint, the residual stress magnitude is approximating around 90-100% of the yield strength magnitude of the material at room temperature. Moreover, compressive stresses existed in the first weld bead while, tensile stresses were found in the second weld bead of a tee section weld joint. The influence of key weld parameters on weld joint quality was investigated experimentally by Jia et al. [15]. Moreover, the authors developed a 3D model for performing welding simulation. The simulation complexity is minimised by carrying out a sensitivity analysis for the heat source model variables. In fact, different analysis techniques such as partial least-square regression analysis and multiple regression analysis were employed for comparison purpose and evaluating overall weld performance.

Cho et al. [16] carried out a numerical investigation on the effect of double pass V-groove arc welding at different positions. The parameters such as pressure of

arc, input thermal flux and electromagnetic force were examined by Abel invention method using computational fluid dynamics (CFD) technique. From welding simulations, the authors determined that the molten metal pool is affected by gravity and fluctuate with position across transverse sections in weldment. Heinze et al. [17] examined the influence of multi-pass arc welding in 20 mm thick structural steel on residual stress distribution using numerical simulation under free shrinkage criterion. The results demonstrated that there was a steep rise in residual stress magnitude up to 400MPa across transverse direction in structural steel weldments. Cho et al. [18] investigated the molten pool behaviours in V-groove arc weldments joined with and without incorporation of root gap in flat, overhead and vertical positions. It is observed that an incomplete penetration is formed in weldments when root gap in flat and overhead position is considered. However, there is overflow of molten metal when root gap of 1 mm is considered. Lu et al. [19] developed a self-consistent 3D model to investigate the energy flow in aluminium alloy during metal arc welding process. The numerical model is developed for simulation of bead-on-plate welding with an objective to predict weld profile and compute preferable fluid flow motion in melt pool by considering various weld parameters. Jaime et al. [20] has studied the relationship between weld parameters and bead area geometry in arc welding process. From the experimental results, the authors observed that the process parameters have an influence on bead area. Therefore, further mathematical models were developed from the experimental data to estimate weld dimension within 0-20% accuracy.

Rao et al. [21] have developed mathematical model for arc welding process and employed different welding conditions to achieve stability in GTAW process. The welding conditions are varied during electrode melting which involves droplet formation, detachment and transfer from electrode. Moreover, the effect of plasma arc and wire-feed-speed variation on weld joint quality is determined. Based on experimental results, it has been determined that the electrode melting is a result of Joule heating and arc generation, and the feed rate of wire should dynamically balance with the melting rate of electrode for attainment of a stable welding process. Wang et al. [22] have developed a 3D process model to simulate the metal transfer process during arc welding. The numerical model will take into account the effects of effective-viscosity, enthalpy and volume-of-fluid. The authors examined the shape of the droplet during melting at the interface of the wire, droplet oscillation at the tip of the wire, physical variables characteristics and its function. Wang et al. [23] investigated the fluid dynamics of droplets impinging from filler material into weld pool during spot arc welding through numerical modelling technique. The authors numerically computed the combined effects of surface tension force and momentum of droplet impingement force on weld profile formation and complex fluid flow characteristics in the melt pool at different time segments. In fact, the authors have analysed that to numerically simulate the metal transfer process during arc welding process an advanced Computational fluid dynamics (CFD) technique is recommendable. It involves a two-step projection procedure for computing fluid flow of incompressible nature. The first step is free surface capture through volume of fluid (VOF) method and the second step is computing the force generated due to surface tension through continuum surface force (CSF) model.

In spite of having several ongoing researches on the development of mathematical modelling and computational methods for similar plate thickness during arc welding process that are highly efficient and capable of estimating temperature distribution, weld profile, metal transfer and fluid flow effects. However, researches undertaken to comprehend the complex behaviour of temperature distribution, weld

profile formation using numerical method for dissimilar plate thickness during arc welding process is absent in literature. Therefore, in the present work, a thermal analysis on single-pass butt welding were carried out for SS304 dissimilar sheets of 2.5 mm and 4 mm thicknesses. Moreover, double-ellipsoidal power density model and material properties with respect to temperature variable has been employed to estimate temperature distribution and weld profile formation during welding procedure. The output responses of thermal analysis such as temperature distribution is validated against experimental data.

2. THEORETICAL BACKGROUND

The conduction based thermal modeling is preferable due to ease of modeling, reduce amount of computational time and easy coupling during structural analysis. The effect of convective heat transport within the weld pool is taken into account by substituting a preferable volumetric power density model in finite element (FE) based thermal model. Moreover, an artificial enhancement of thermal conductivity at molten material state is being done to incorporate the action of convective heat transmission process of molten metal in liquidus state. The finite element based thermal analysis for arc welding process follows the principle of conservation of energy which is based on Fourier law of heat conduction equation. If the welding takes place along Y axis direction with a velocity 'v' then the governing heat conduction equation in terms of Cartesian coordinate system is mathematically represented as

$$k\left(\frac{\partial^2 T}{\partial x^2}+\frac{\partial^2 T}{\partial y^2}+\frac{\partial^2 T}{\partial z^2}\right)+Q_{\text{int}}=\rho c_p\left(\frac{\partial T}{\partial t}-v\frac{\partial T}{\partial y}\right) \quad (1)$$

Where k represents thermal conductivity, C_p denotes specific heat, ρ represents density, Q_{int} refers to the internal heat generation rate, T denotes temperature variable, t specifies time and v is welding velocity. While x, y and z refer to coordinates along transverse, longitudinal and thickness direction of the weldment. The welding process involves heat input from a specified thermal source and heat exchange between the welded plate and its surroundings through convection and radiation heat losses with subsequent cooling process. Fig.4 represents schematic of applied boundary conditions on the solution domain.

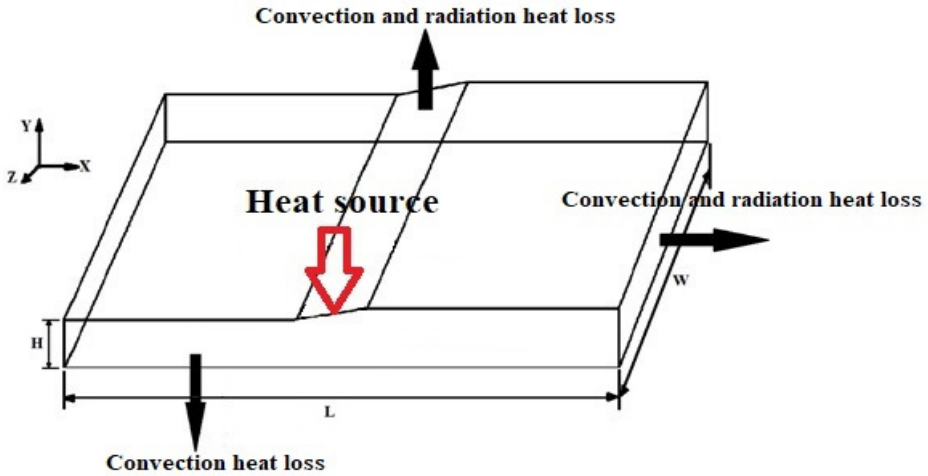

Figure 4: Schematic representation of boundary conditions on the solution domain.

In thermal analysis, heat losses in the form of convection and radiation heat transfer are referred as dynamic boundary conditions. These are mathematically represented as

$$q_c = h(T - T_0) \tag{2}$$

$$q_r = \sigma \times \varepsilon (T^4 - T_0^4) \tag{3}$$

Where q_r and q_c refers to radiation and convection heat transfer, T_0 signifies initial or pre-heat or inter-pass temperature. However, in the present work T_0 is defined as reference temperature which is considered as 300K; σ represent Stefan–Boltzmann constant which is 5.67×10^{-8} W m^{-2} $°C^{-4}$; h is convection heat transmission coefficient, ε is the emissivity (0.9) of the work piece material. In the present work, Goldak's double ellipsoidal power density model is considered as welding heat input for welding simulations. Fig. 5 represents schematic of double ellipsoidal power density model.

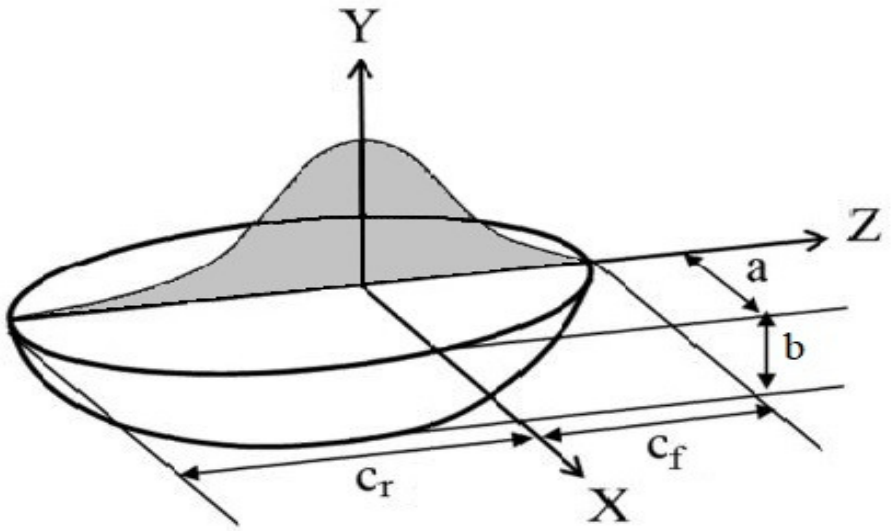

Figure 5: Representation of double-ellipsoidal volumetric power density model.

In double ellipsoidal power density model, the energy density in the front and rear section is asymmetrically distributed due to influence of welding velocity and power density. In case, the welding heat source is traversing along Y-axis direction then the energy density distribution at front section of double ellipsoidal power density model is mathematically expressed as:

$$q_f(x,y,z) = \frac{6\sqrt{3}(f_f Q_{\text{int}})}{abc_f \pi^{3/2}} \exp[\frac{-3x^2}{a^2} + \frac{-3y^2}{b^2} + \frac{-3z^2}{c_f^2}]; z \geq 0 \tag{4}$$

Where a, b, and c_f are ellipsoidal model parameters and f_f is the proportion of heat deposited in the front section. Similarly, the heat flux equation for rear section of double ellipsoidal power density model is mathematically represented as:

$$q_f(x,y,z) = \frac{6\sqrt{3}(f_r Q_{\text{int}})}{abc_r \pi^{3/2}} \exp[\frac{-3x^2}{a^2} + \frac{-3y^2}{b^2} + \frac{-3z^2}{c_r^2}]; z \leq 0 \tag{5}$$

Where a, b, and c_r are ellipsoidal model parameters and f_r is the proportion of heat deposited in the rear section. The heat intensity Q_{int} which denotes actual heat input from the heat source is mathematically represented as

$$Q_{\text{int}} = \eta P \text{ or } Q_{\text{int}} = \eta IU \tag{6}$$

Where P, I, η and U and represents arc power, welding current, arc efficiency and arc voltage respectively. The proportion of heat deposited must satisfy the following relation

$$f_f + f_r = 2 \tag{7}$$

In the present analysis, the efficiency of arc is defined as 0.6. In fact, the heat flux generated by arc on substrate surface is substituted with a double-ellipsoidal power density model [24-28].

3. RESULTS AND DISCUSSION

Single-pass butt aligned arc welding experiments were performed by Hashemzadeh et al. [29] using austenitic stainless steel plates of dimensions 150 × 400 × 2.5 mm^3 and 150 × 400 × 4 mm^3. In their work, the authors obtained a bead length of 400 mm and reported time-temperature characteristics at different locations during arc welding of austenitic stainless steel in butt aligned configuration. The process parameters employed for single-pass welding operation during experiments are presented in Table 3. In the present analysis, the process parameters are selected for comparison purpose and for validation of the developed process model. Although the authors have consider the data from literature, the plasma arc welding process also verified with the same model. During welding operation, eight points were selected for the measurement of temperature distribution in butt aligned plates of different thicknesses. Three thermocouples were fixed at the top surface of each plate from the weld centreline at a distance of 10 mm, 20 mm and 30 mm away respectively. While for the bottom surface, thermocouple readings were recorded at a span of 10 mm away from the weld centreline corresponding to each plate. The schematic representation of position of thermocouple at the top and bottom surfaces of the weldment in butt aligned plates is presented in Fig. 6. To measure the temperature histories 'K type' thermocouple was utilized. The temperature data were recorded at the selected points by Armature Multiplexer Module 34901A and Agilent 34970A Data Acquisition/Switch Unit at an interval of 2s.

Table 3: Weld parameters employed during experimental operation [29].

Parameters	Values	Units
Welding current, I	233	A
Travel speed, v	6	mm s^{-1}
Power, P	2330	W

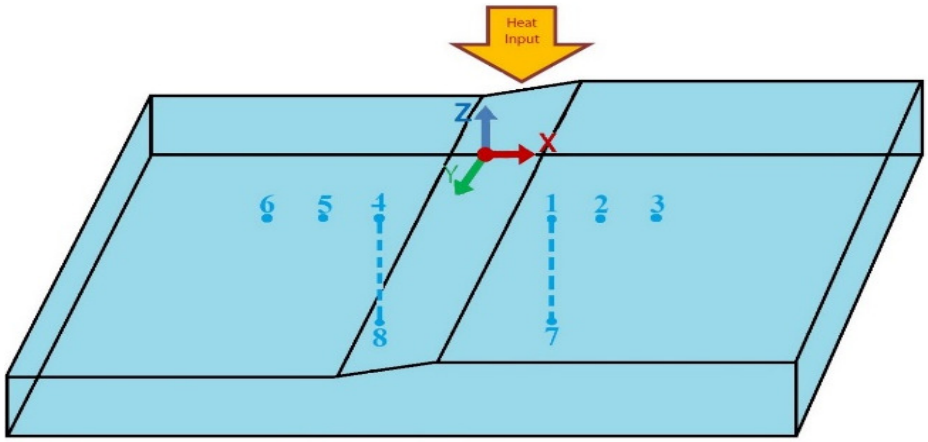

Figure 6: Thermocouple locations in butt aligned dissimilar plates.

The temperature measurement locations in butt aligned austenitic stainless steel plates of different thicknesses corresponding to X, Y and Z axis direction for FE model is presented in Table 4. The temperature values were evaluated at 16.28, 26.06 and 35.85 mm respectively from the weld centerline on the surface of 4 mm plate thickness. And, at -9.78, -19.56 and -29.35 mm respectively from the weld centerline on surface of 2.5 mm plate thickness. While, at the bottom surface the temperature magnitude was determined at a span of 16.28 mm from the weld centerline for 4 mm plate thickness & at a span of -9.78 mm from the weld centerline for 2.5 mm plate thickness.

The accuracy and effectiveness of the developed finite element based thermal model relies on incorporation of appropriate temperature dependent material properties, boundary constraints, mesh distribution over the solution domain and other model parameters. In fact, the accuracy of the computational result will improve and the time span for processing will reduce if a refine mesh is defined at and near the weld centerline and a gradual coarse mesh is incorporated away from the weld zone. Moreover, specific heat capacity and thermal conductivity are the core temperature dependent material properties that have an effect on the final outcome of thermal analysis. However, material properties such as emissivity and density does not have much influence on the thermal analysis outcome since, these properties magnitude remain almost constant with respect to temperature. Thermal conductivity, density and specific heat capacity of austenitic stainless steel material with respect to temperature which are employed for numerical simulation during arc welding process is specified in Table 5.

Table 4: Temperature measurement locations in butt aligned austenitic stainless steel plates of different thicknesses corresponding to numerical analysis.

Thermocouple	X-Coordinate	Y-Coordinate	Z-Coordinate
1	16.28	4	-149.9
2	26.06	4	-149.9
3	35.85	4	-149.9
4	-9.78	2.5	-149.9
5	-19.56	2.5	-149.9
6	-29.35	2.5	-149.9
7	16.28	0	-149.9
8	-9.78	0	-149.9

Table 5: Temperature dependent thermal properties of austenitic stainless steel material used in the present work [28].

Temperature (K)	Thermal conductivity (W/ m K)	Density (kg m^{-3})	Specific heat (J/ kg K)
273	14.6	7900	462
373	15.1	7880	496
473	16.1	7830	512
573	17.9	7790	525
673	18	7750	540
873	20.8	7660	577
1073	23.9	7560	604
1473	32.2	7370	676
1573	33.7	7320	692
1773	120	7320	935

The transient thermal analysis is carried out using ANSYS Parametric Design Language for the development and simulation of a FE based heat transfer model. SOLID 70 element type is selected for heat transfer analysis. It is an eight nodded solid element and temperature is considered as degree of freedom corresponding to each node. Moreover, SOLID 70 can be employed for 3D transient or steady-state thermal analysis. In fact, the heat transmission process within the melt pool for constant velocity field during mass transport analysis can be easily be computed using SOLID 70 element. The schematic representation of element SOLID 70 is depicted in figure 7.

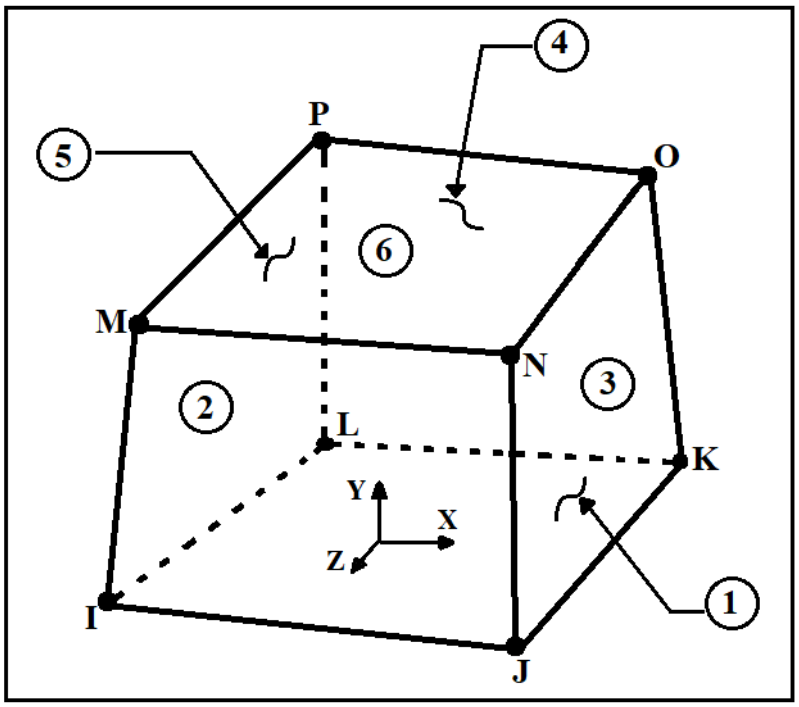

Figure 7: Geometry of SOLID70 element used in finite element modelling.

Figure 8 outlines the basic steps involved in conduction based heat transfer analysis by means of volumetric heat source during the present work. The overall basic steps are listed out as follows,

(i) Initially the model geometry is created in finite element software and thereby the solution domain is discretized into a number of elements such that the mesh generated is refined in close proximity to the heat source while coarser away from it.

(ii) Subsequently, the thermal properties of the material as a function of temperature are stated along with welding process parameters. Then, the initial and thermal boundary constraints along with volumetric heat source model is defined. Eventually, the volumetric heat source is applied and the model parameters are incorporated.

(iii) The transient heat transfer analysis is performed by dividing the total weld time into smaller time frames and the heat transfer analysis for each smaller time frame explicitly is executed.

(iv) The output of conduction based heat transfer analysis is nodal temperature at each time-sub step (every small interval and each location). From these nodal temperatures, output responses such as weld bead profile and dimensions can be obtained.

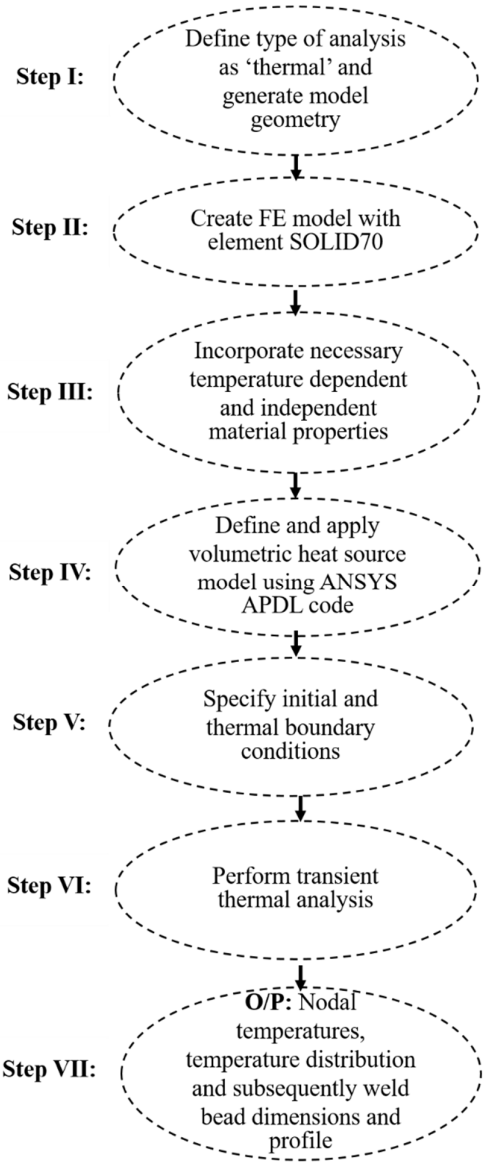

Figure 8: A detailed solution strategy of thermal analysis.

The thermal analysis for butt aligned plates of different thicknesses is performed in ANSYS 14.0 software which is established on FE method. The model dimension of austenitic stainless steel plates for numerical analysis are same as plate dimension used during experimental operation. Moreover, in order to approximate the effect of convective heat transport within melt pool, the volumetric heat source is often used in conduction based heat transfer model. The thermal conductivity of the molten material is increased artificially in several folds to account the enhanced heat transfer due to high convective flow of liquid molten metal within the weld pool [28]. Initially, the FE model geometry is created in FE software. Thereby, a non-uniform mesh model is created in which the entire geometric model is discretized into a number of small elements. Such that; a refine mesh is generated at and near the weld zone while a gradual coarse mesh is incorporated away from the weld domain. Subsequently, thermal properties as a function of temperature along with welding process parameters are defined. Also, initial and thermal boundary constraints are

defined along with appropriate thermal model. Eventually, double ellipsoidal power density model is applied and model parameters are incorporated. The transient thermal analysis is performed by dividing the total weld time into smaller time frames and thermal analysis is executed for each time frames explicitly. The outcome of thermal analysis is nodal temperature corresponding to individual time sub-steps viz. at each location and every small interval. From nodal temperature, other output responses such as weld dimensions and profile is estimated. Fig. 9 presents a meshed FE model while fig. 10 presents zoomed-in view of FE model demonstrating fine mesh at the weld joint and a gradual increase in mesh size away from the weld area.

The numerical simulations were performed for different welding parameter set corresponding to Table 1. Fig. 11 presents temperature distribution of austenitic stainless steel weldment at different time sub steps corresponding to 2330 W arc power and 6 mm s^{-1} welding speed. It can be observed that the weld zone and HAZ is defined by different colors which is represented in temperature isotherm bar. The red color region in the temperature isotherm bar depicts that the temperature is well above the liquidus temperature of austenitic stainless steel base metal which is 1723 K. The temperature range in isotherm contour where molten weld metal deposition transpire is from 1673 K to 1723 K. The temperature isotherm for HAZ lies in between 1173 K and 1473 K and most of the solid state transformation prevails within this temperature range. Moreover, the numerical results denotes that conduction based heat transfer analysis is capable of predicting accurate temperature distribution in deep penetration arc welding process. Fig. 12 represents numerically computed cross-sectional view of austenitic stainless steel weldment corresponding to 2330 W arc power and 6 mm s^{-1} welding speed. The weld width and penetration is determined as 4.56 mm and 2.91 mm. The weld profile of austenitic stainless steel weldment represents funnel shaped at 2330 W arc power and 6 mm s^{-1} welding speed.

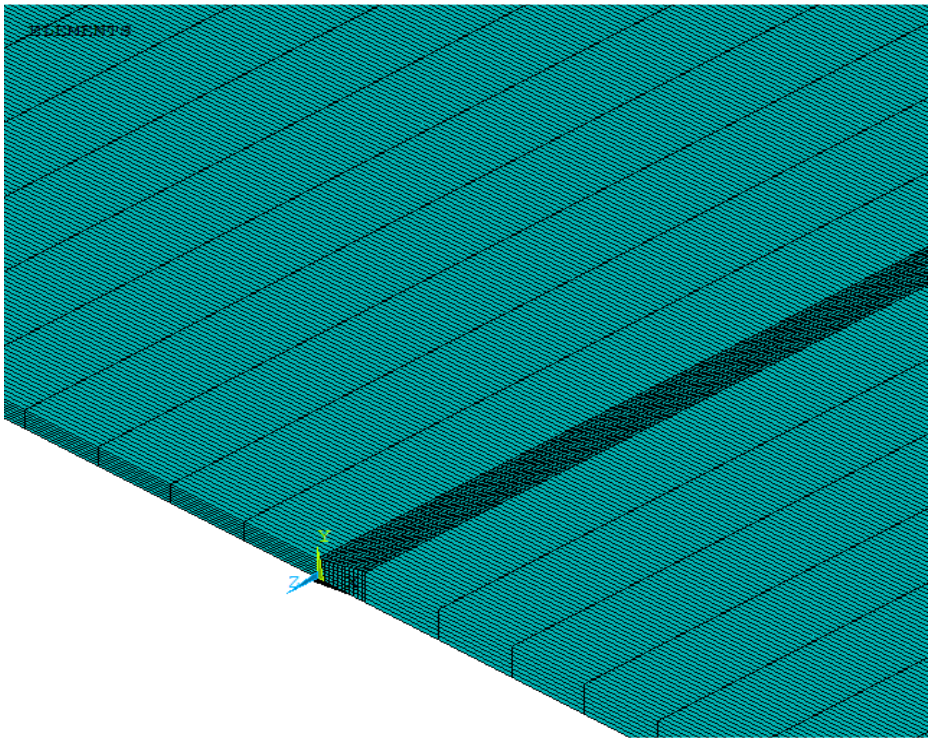

Figure 9: Presentation of meshed finite element model.

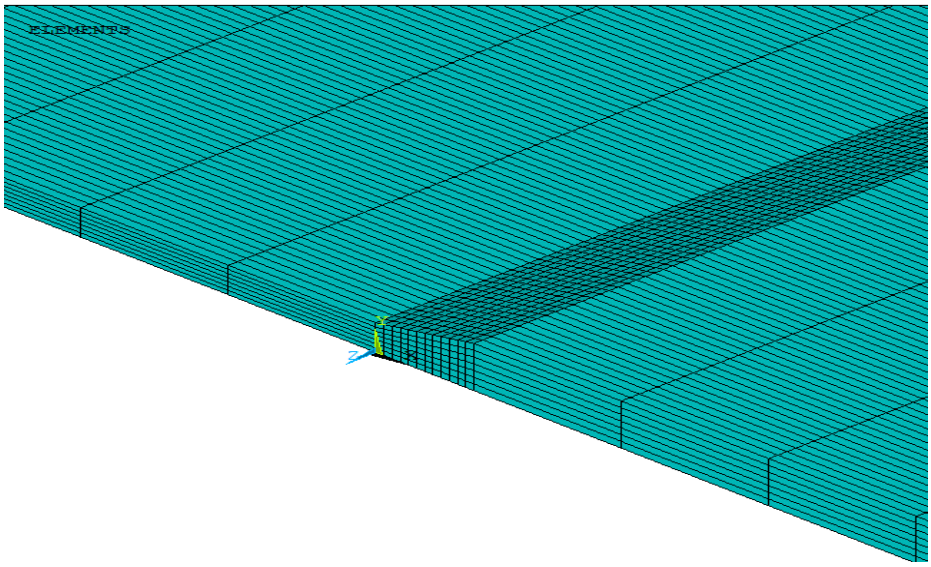

Figure 10: Presentation of zoomed- in view of FE model with refine mesh distribution at the weld area and a gradual coarse mesh distribution away from the weld area.

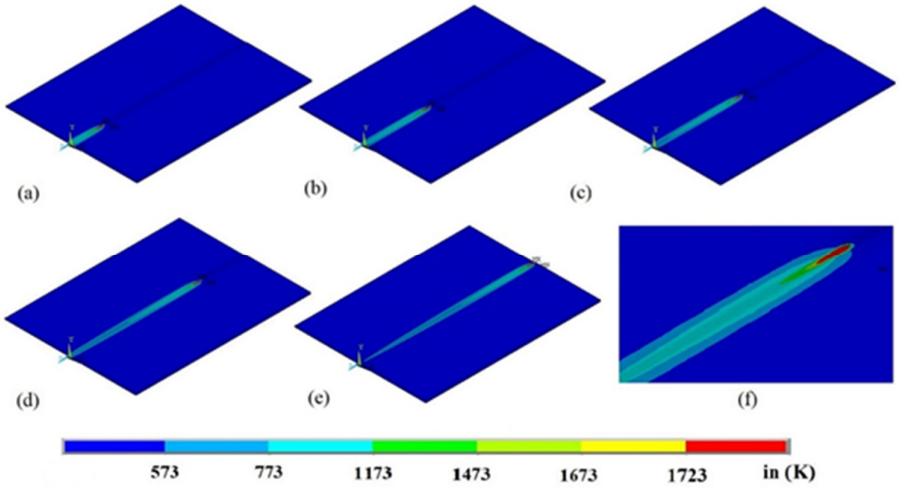

Figure 11: Temperature distribution across the weld pool of austenitic stainless steel weldment at different time sub-steps corresponding to 2330 W arc power and 6 mm s-1 welding speed.

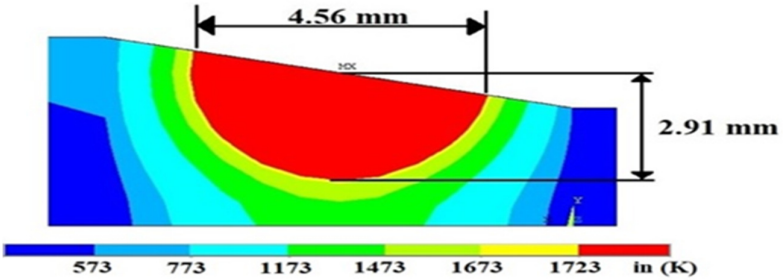

Figure 12: Numerically computed cross sectional view of austenitic stainless steel weldment corresponding to 2330 W arc power and 6 mm s-1 welding speed.

Fig. 13 shows the time temperature history of thermocouple corresponding to six different locations as presented in Table 2 for butt aligned austenitic stainless steel plates of different thickness. From the graph, it can be observed that for 2.5 mm thickness plate at -9.78 mm location and for 4 mm thickness plate at 16.28 mm location, there is a sharp rise and fall in temperature with respect to time variable. The sudden rise and fall in temperature is due to heat source movement towards and away from the measured point locations. Also, the temperature distribution trend signifies that the peak temperature attained and cooling rate is higher near the weld zone of 2.5 mm plate thickness than that of 4 mm plate thickness. Since, the temperature measurement location is near to the weld zone of 2.5 mm thickness plate. Furthermore, from the plot it is recognised that with increase in distance from the weld centre corresponding to 2.5 mm and 4 mm thickness plate, the temperature distribution curve declines with respect to time variable.

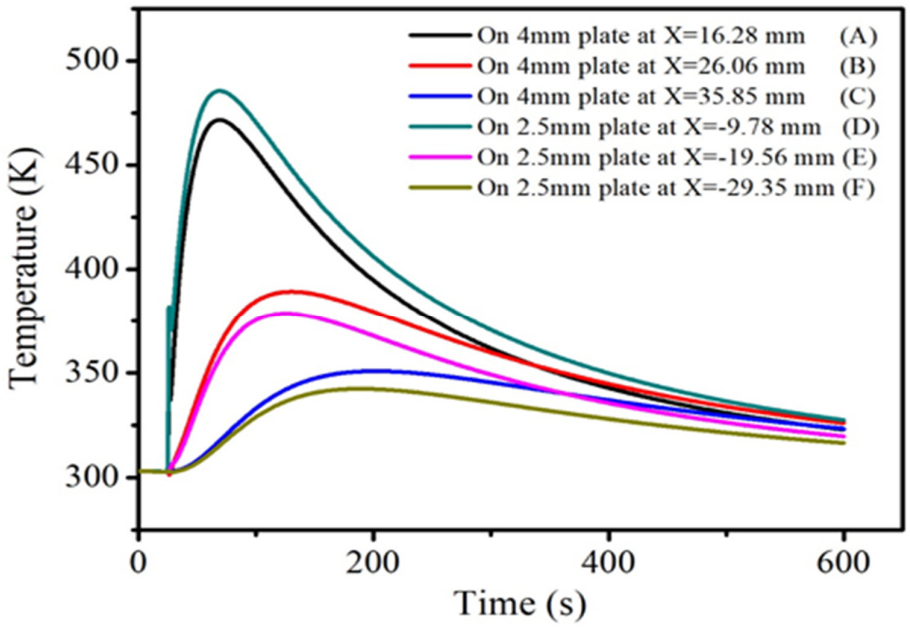

Figure 13: Numerically determined time temperature history corresponding to six different locations in butt aligned austenitic stainless steel plates of different thickness.

Fig. 14 represents numerically determined cross-sectional macrographs of austenitic stainless steel weldment at constant welding speed and at two different arc power. It is determined that the weld width and penetration is increased with rise in power from 1830-2330 W while other parameters are kept constant. While, figure 15 represents numerically determined cross sectional view of austenitic stainless steel weldment at a constant arc power of 2330 W and different welding speed. However, in this case it is determined that at constant arc power, weld width is decreased with increasing welding speed from 3 mm s-1 to 6 mm s-1 while other parameters are kept constant. From numerical results, it can be derived that the welding speed and arc power governs the weld penetration and width for arc welding process.

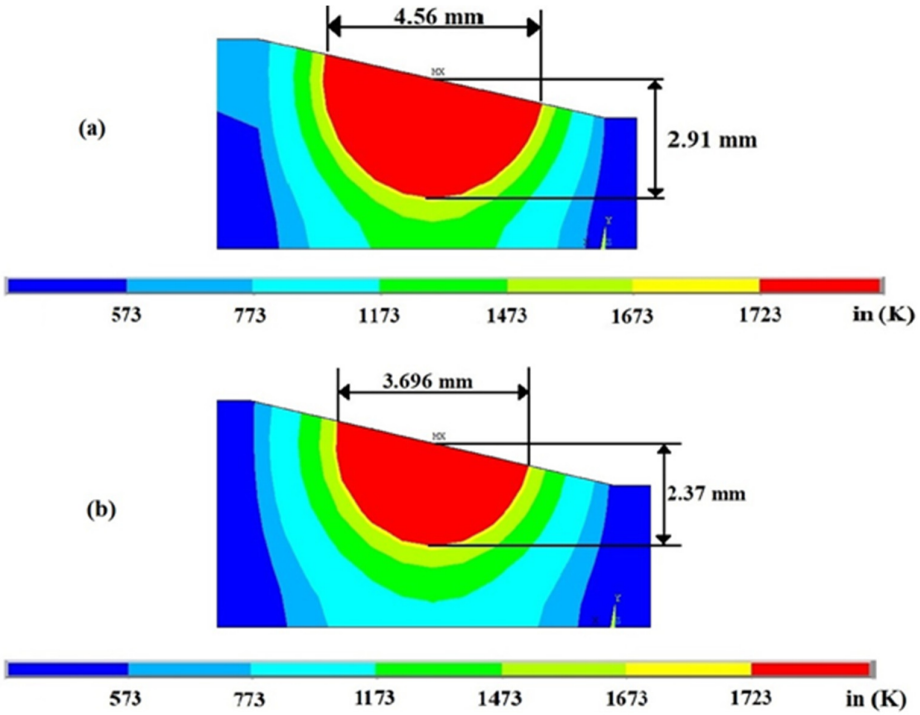

Figure 14: Numerically determined cross sectional image of austenitic stainless steel weldment at constant welding speed of 6 mm s^{-1} and at arc power of (a) 2330 W and (b) 1830 W.

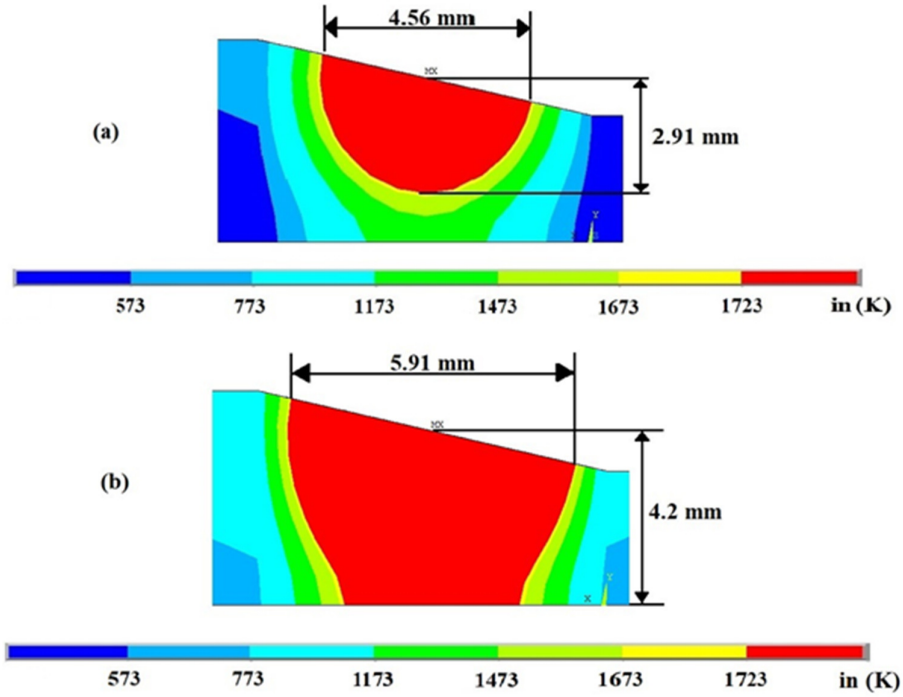

Figure 15: Numerically determined cross sectional view of austenitic stainless steel weldment at a constant arc power of 2330 W and at welding speed of (a) 6 mm s^{-1} and (b) 3 mm s^{-1}.

Figure 16 and 17 presents the time temperature history of the experimental data extracted from literature [19] and the numerically determined result of the points corresponding to both the sides of the weld joint from the weld line at the top and

bottom surface respectively. From Fig. 16 (a), it can be observed that for 2.5 mm and 4 mm plate thicknesses, the maximum temperature magnitude is 753 K and 671 K at a span of 10 mm from the weld line. While in Fig. 16 (b), the temperature rise at a span of 9.87 mm from the weld line of 2.5 mm plate thickness is 487 K and at a span of 16.28 mm from the weld line of 4 mm plate thickness the peak temperature magnitude is 473 K. From Fig. 16(a) and (b), it can be identified that there is a steep rise in temperature distribution curve for 2.5 mm thickness plate as against 4 mm thickness plate corresponding to experimental data and numerically determined result. The above data suggest that heat transmission due to conduction is faster in case of lower thickness plate when compared with higher thickness plate. Moreover, from the plots it is spotted that with increase in distance from the weld centre, the temperature distribution curve falls corresponding to 2.5 mm and 4 mm thickness plates. Since, the effect of heat source on temperature magnitude is maximum at and near the weld centre and it diminishes with increase in distance from the weld location. In fact, the % error between temperature distribution corresponding to experimental data and numerically determined result is less than 10 which demonstrates that the validation of experimental data against numerically computed results is fair enough. Moreover, it also signifies the efficacy of the developed process model.

Fig. 17 (a) represents plot of experimental data at a span of 10 mm from the weld line on the bottom surface of austenitic stainless steel weldment. The maximum temperature attained corresponding to 2.5 mm and 4 mm plate thickness is 698 K and 609 K at a span of 10 mm away from the weld line. While Fig. 17 (b) presents numerically computed results at a span of 9.87 mm from the weld line for 2.5 mm plate thickness and at a span of 16.28 mm from the weld line for 4 mm plate thickness on the bottom surface of austenitic stainless steel weldment. The peak temperature attained is determined as 487 K and 473 K for 2.5 mm and 4 mm thickness plates. The temperature distribution pattern in Fig. 15 follows the same trend as in Fig 16. Whereby, temperature magnitude curve is higher in case of 2.5 mm thickness plate as against 4 mm thickness plate due to higher heat conduction transmission rate. And, also with increase in distance from the weld centre corresponding to 2.5 mm and 4 mm thickness plates the temperature magnitude declines. It is due to heat source movement along longitudinal direction and temperature measurement location is across transverse direction of the weld zone.

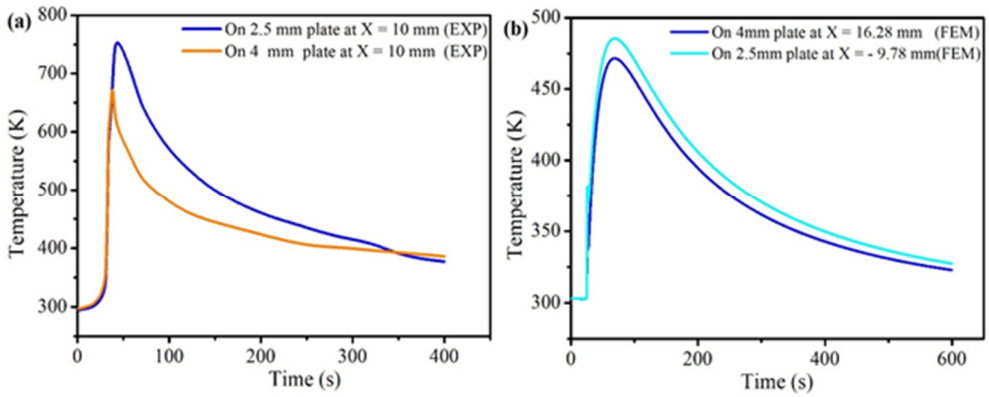

Figure 16: Time temperature history at the points corresponding to both the sides of the weld joint from the weld line at the top surface for (a) experimental data and (b) numerically determined result.

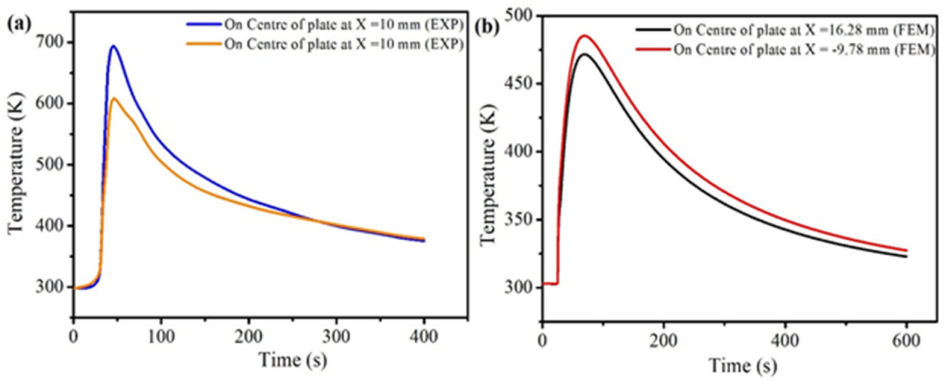

Figure 17: Time-temperature history at the points corresponding to both the sides of the weld joint from the weld center at the bottom surface for (a) experimental data and (b) numerically determined result.

4. CONCLUSION

Metals such as SS, Ti-alloy are used in biomedical applications. Moreover, the application of welding processes are prominent in biomedical applications for making biomedical devices and human implant at different locations. In the present study, a FE based thermal model is developed using double ellipsoidal power density model for arc welding technique. Though, the analysis can further be extended to estimate mechanical behaviour of biomedical metal welds in future works. Moreover, the following are the conclusions drawn from the present work:

• The influence of the welding current, voltage and speed is studied in detail by comparing the maximum temperature and change in the weld profile under the different process parameters.

• Double-ellipsoidal power density model of Gaussian distribution is employed to estimate temperature distribution in austenitic stainless steel weldments of different plate thicknesses.

• The temperature distribution at different weld locations on top and bottom surface is numerically computed and validated against experimentally measured data points. It is determined that the temperature magnitude is higher near the weld zone location due to heat source movement along the longitudinal direction.

• The temperature magnitude is higher in case of 2.5 mm thickness plate when compared with 4 mm thickness plate due to higher heat conduction transmission rate in 2.5 mm thickness plate.

References:

[1] M. Merola, A. Saverio, Materials for hip prostheses: a review of wear and loading considerations, Materials, 12 (3), 495 (2019).

[2] C. P. Bergmann, A. Stumpf, Biomaterials. In: Dental Ceramics: Microstructure, Properties and Degradation. Topics in Mining, Metallurgy and Materials Engineering. Springer Berlin Heidelberg, Berlin, Heidelberg, 2013, 9.

[3] S. A. Rodrigues, A. G. C. Presotto, V. A. R. Barão, R. L. X. Consani, M. A. A. Nóbilo, M. F. Mesquita, The role of welding techniques in the biomechanical behavior of implant-supported prostheses, Mater. Sci. Eng. C, 78, 435 (2017).

[4] C. Fornaini, M. Meleti, M. Bonanini, G. Lagori, P. Vescovi, E. Merigo, S. Nammour, Laser Welded versus Resistance Spot Welded Bone Implants: Analysis of the Thermal Increase and Strength, Scientific World J., (2014) 8.

[5] J. Paek, H. W. Ahn, D. M. Jeong, J. S. Shim, S. H. Kim, K. R. Chung, Application of the 2-piece orthodontic C-implant for provisional restoration with laser welded customized coping: a case report, Head Face Med. 11 (2015) 7.
[6] Y. Suzuki, C. Ohkubo, M. Abe, T. Hosoi, J. Prosthet. Dent., 91 (5) (2004) 418.
[7] S. Prasad, E. A. Monaco, J. Prosthodont. Dent., 101 (4) (2009) 221.
[8] Y. M. Lin, G. Q. Jiang, J. L. Calderon, Laser Welding Assembling of an Implantable Bio-Medical Device: Investigation of Temperature Field, in: Laser-Based Micro- and Nano-packaging and Assembly V, Spie-Int Soc Optical Engineering, Bellingham, 2011.
[9] K. H. Wang, G. Liu, J. Zhao, J. L. Wang, S. J. Yuan, Mater. Des. 91 (2016) 269.
[10] W. V. Vaidya, M. Horstmann, V. Ventzke, B. Petrovski, M. Kocak, R. Kocik, G. Tempus, J. Mater. Sci., 45 (22) (2010) 6242.
[11] I. A. Ibrahim, S. A. Mohamat, A. Amir, A. Ghalib, Procedia Eng., 41 (2012) 1502.
[12] H. Guo, J. Hu, H. L. Tsai, Int. J. Heat Mass Transf. 52 (2009) 5533.
[13] G. Xu, J. Hu, H. L. Tsai, Int. J. Heat Mass Transf. 52 (2009) 1709.
[14] J. D. Francis, Welding Simulations of Aluminum Alloy Joins by Finite Element Analysis, PhD Dissertation, Virginia Polytechnic Institute and State University, 2002.
[15] X. Jia, J. Xu, Z. Liu, S. Huang, Y. Fan, Z. Sun, Fusion Eng. Des. 89 (2013) 40.
[16] C. Heinze, C. Schwenk, M. Rethmeier, Mater. Design 35 (2012) 201.
[17] D. W. Cho, S. J. Na, M. H. Cho, J. S. Lee, J. Mater. Process. Technol. 213 (2013) 1640.
[18] F. Lu, H. P. Wang, A. B. Murphy, B. E. Carlson, Int. J. Heat Mass Transf. 68 (2013) 223.
[19] D. R. Jaime, I. L. Juarez, P. Perez, Procedia Technol. 7 (2013) 398.
[20] Z. H. Rao, J. Zhou, H. L. Tsai, Inter J. Heat and Mass Transf. 55 (2012) 6651.
[21] F. Wang, W. K. Hou, S. J. Hu, E. K. Asibu, W. W. Schultz, P. C. Wang, J. Phys. D: Appl. Phys. 36 (2003) 1143.
[22] Y. Wang, H. L. Tsai, Int. J. Heat and Mass Transf. 44 (2001) 2067.
[23] G. Wang, P. G. Huang, Y. M. Zhang, Metall. Mater Trans. 34 (2003) 345.
[24] N. Yadaiah, S. Bag, C. P. Paul, L. M. Kukreja, Int. J. Adv. Manuf. Technol. 86 (1) (2016) 853.
[25] N. Yadaiah, S. Bag, Int. J. Thermal Sci. 86 (2014) 125.
[26] S. Chowdhury, N. Yadaiah, M. Muralidhar, Proceedings Institution Mechanical Eng. Part C: J. Mechanical Eng. Sci. 233(18) (2019) 6602.
[27] S. Singh, N. Yadaiah, S. Bag, S. Pal, Proceedings Institution Mechanical Eng. Part C: J. Mechanical Eng. Sci. 228(16) (2014) 2960.
[28] N. Yadaiah, S. Bag, ISIJ Int. 52(11) (2012) 2069.
[29] M. Hashemzadeh, B. Q. Chen, C. G. Soares, Intern. J. Adv. Manuf. Tech. 78 (2014) 319.